Optically driven control of mechanochemistry and fusion dynamics of biomolecular condensates via thymine dimerization

Vahid Sheikhhassani[1,2], Faith F.H.K. Wong[1,2,3], Daniel Bonn[4], Jeremy D. Schmit[5], Alireza Mashaghi[1,2,*]

[1] Medical Systems Biophysics and Bioengineering, Division of Systems Pharmacology and Pharmacy, Leiden Academic Centre for Drug Research, Leiden University, Leiden 2333CC, The Netherlands

[2] Laboratory for Interdisciplinary Medical Innovations, Centre for Interdisciplinary Genome Research, Leiden University, Leiden 2333CC, The Netherlands

[3] Department of Life Sciences, Faculty of Natural Sciences, Imperial College London, London SW72AZ, UK

[4] Van der Waals-Zeeman Institute, Institute of Physics, University of Amsterdam, Amsterdam 1098XH, The Netherlands

[5] Department of Physics, Kansas State University, Manhattan, KS 66506, USA

*Correspondence: a.mashaghi.tabari@lacdr.leidenuniv.nl

Abstract

Phase-separated biomolecular condensates serve as functional elements of biological cells, as contributors to the formation of protocells in prebiotic systems during early life, and as a distinct form of material with a range of applications. Regulation of condensate mechanochemistry is of critical importance for their functions and properties. Photochemical processes, such as UV-induced chemical changes, are commonly observed in nature and can have both detrimental and constructive impacts on life, and are also readily implemented in engineering applications. However, how phase-separated condensate formation influences photochemical processes, and conversely, how photochemical reactions impact condensate dynamics, remains an open question. Combining scanning probe microscopy with optical imaging and control, we developed a first-of-its-kind assay that enables the study of mechanical transitions and fusion dynamics in condensate droplets, revealing that UV-induced thymine dimerization alters condensate nucleation and coalescence. Depending on the exposure and topological arrangement of thymine dimers, UV can induce a transition from liquid-like to solid-like behaviours or lead to aggregate formation. UV treatment also leads to compartmentalization in condensate systems by e.g., promoting the formation of arrested fusion droplets, which are stable against environmental changes. UV illumination can thus be leveraged to program the architecture and material properties of DNA-based biomolecular condensates, with implications for genome biology, the emergence of life on Earth, and engineering applications.

Introduction

Biomolecular condensates formed through liquid-liquid phase separation (LLPS) play key roles in various cellular processes, ranging from gene regulation to stress granule formation [1–5]. These condensates, which assemble through multivalent interactions among macromolecules such as nucleic acids and proteins, exhibit a wide range of mechanical properties, which are directly linked to their function[6,7]. The strength, density, and topological arrangement of interactions, along with mechanical properties of the polymer chains, are critical determinants of condensation and the resulting mechanical phenotype[8]. External triggers are known to modulate molecular conformations and interactions, potentially altering the phase separation process [9]. Modulation of the mechanical properties of condensates is typically achieved by introducing new molecules (e.g., crosslinkers) or adjusting molecular concentrations - approaches that inherently alter condensate composition, making it difficult to disentangle the effects of mechanics and chemistry[10].

One key external trigger that significantly influences cellular processes is ultraviolet (UV) radiation, which is both a major cause of DNA damage through the formation of covalently bonded pyrimidine dimers such as thymine dimers (TT) and a critical factor in the emergence of life on Earth[11,12]. TT dimers disrupt normal DNA replication[13] and transcription[14], leading to mutations that can initiate various diseases, and are the primary cause of skin cancer[15]. The cellular machinery recognizes and attempts to repair these lesions via mechanisms like nucleotide excision repair[16]; however, persistent or improperly repaired TT dimers can give rise to short stretches of single-stranded DNA (ssDNA), ultimately contributing to genomic instability and carcinogenesis[17]. Furthermore, membraneless condensates are proposed as structural components of protocells and are thought to play a critical role in the emergence of life on Earth. Coacervates, formed via liquid-liquid phase separation of building blocks, can grow while the overall internal concentration remains approximately constant[18]. The droplets are permeable to molecules from the surroundings with some selectivity, enabling chemical synthesis and targeting (receptor-ligand) required for life[19]. Nucleic acids, which are known for their propensity to form condensates, are considered key components of protocells[18]. Evidence indicates that photochemical processes play critical roles in the structuring of the building blocks[20]. This is particularly important in the case of coacervates, as they lack lipid membranes and, thus, cannot partially shield solar UV. It remains unclear, however, what UV does to (nucleic acid) coacervates and whether it can shape their structural mechanics.

Elucidating how UV irradiation alters the formation and material properties of phase-separated droplet systems is crucial but challenging. Active microrheological characterization of condensate droplets is mostly performed utilizing optical tweezers (OT)[21,22]. Despite being a powerful approach, introducing UV illumination into current assays is not straightforward. Recently, scanning probe microscopy (SPM) has been applied, which enables the characterization of the material properties of condensates[10]. While techniques such as OT[23] and micropipette aspiration[24,25] have been employed to probe the mechanics of biomolecular droplets, which often require the addition of tracer particles or microscale probes. In contrast, SPM, within a significantly higher range of forces, can directly probe the surface and local internal environment of condensates with minimal perturbation, eliminating the need to include exogenous particles in the system[26]. Furthermore, the approach could, in principle, be extended to study droplet-droplet fusion. However, these capabilities have yet to be realized in practice.

In this work, we introduce a photochemical approach to precisely modulate condensate mechanics using UV-induced thymine dimerization, enabling control over mechanical properties while preserving chemical composition. Using poly-thymine single-stranded DNA (dT40) and poly-L-lysine (PLL) as a model system, we demonstrate how this strategy drives transitions among distinct mechanical states, from liquid-like droplets to more rigid, gel- or solid-like networks. To capture these mechanical changes, we developed the first SPM-based assays, combined with optical imaging, for label-free characterization of condensate mechanics and fusion dynamics. These transitions lead to dramatic changes in fusion behavior, ultimately driving compartmentalization, a process relevant to prebiotic chemistry and bio-inspired materials design. We attribute these observations to the formation and topological arrangement of UV-induced TT dimers, which can be local, long-range, or occur between chains. Our study provides a compelling example in which a photochemical reaction alters the condensed phase, and conversely, condensation modulates photochemical reaction outcomes.

Materials and Methods

Stock solutions preparation

ssDNA oligo of dT40 was purchased from Integrated DNA Technologies (NJ, USA). The dry stocks were reconstituted in RNase-free water. DNA concentration was measured

subsequently using a Qubit spectrophotometer. The DNA stocks were then aliquoted and stored at -20°C for further use. Poly-L-lysine (PLL) hydrochloride with an average molecular weight of 15,000 to 30,000 Da was used in all experiments. The PLL was dissolved in water to prepare stock solutions at 22.4 mg/ml concentration. Based on the average molecular weight of the PLL, the average length of the polymer is estimated to be 150 residues long.

Surface passivation for rheological and droplet-droplet interactions analysis

Condensate samples for phase contrast imaging, mechanical analysis, and droplet-droplet interactions analysis were prepared on TPP Petri dishes. For rheological analysis, dishes were passivated with 1 w/v% BSA (A2153) solution, incubated for 30 min, and washed 5-6 times using RNase-free water. For droplet-droplet interaction analysis, the experimental setup required detaching a droplet from the substrate using the cantilever and positioning it on top of a target droplet for the fusion assay. A combination of Pluronic and BSA passivation was used to enable this experiment. On the Pluronic-coated surface, droplets were loosely bound, allowing easy detachment, whereas on the BSA-coated side, droplets showed stronger adhesion, preventing detachment during the fusion process and enabling complete coalescence on the surface. A guideline dividing the dish in half was drawn on the underside of the petri dish to ensure consistent application of the passivation agents. The dish was securely fixed in position and tilted to approximately 20 degrees. For each passivation, the bottom half of the dish was filled with the corresponding passivation agent up to the guideline, incubated for 30 minutes, and washed multiple times by carefully adding RNase-free water.

Sample preparation

Each time, for sample preparation, 60 μL of the working buffer (150 mM KCl (p9333), 10 mM imidazole (56750), and 0.01% w/v NaN_3 (8.22335)[23] were placed as a round droplet at the center of the dish. For droplet-droplet analysis, this step was performed carefully to align the droplet's middle axis with the drawn guideline. To mimic the intracellular environment, the crowding agent Ficoll® PM 70 (F2878) was added to the buffer at a final concentration of 50 g/L. Subsequently, ssDNA and poly-L-lysine (PLL, P2658) were added sequentially to

reach a final concentration of 30 µM for each. After adding each component, the solution was gently mixed by pipetting 10 times.

SPM measurements

A JPK CellHesion 200 (Bruker, Germany) equipped with a phase contrast microscope delivering real-time *in-situ* images of measurements utilizing a 20X/0.4 objective was employed in this study. Mechanical analysis was performed as explained by Naghilou et al.[10] Briefly, a 60 µl bulk drop containing the condensates was prepared, and the droplets were allowed to settle on the dish. All experiments were performed within 4 h of droplet formation. Before each mechanical measurement, a 5 µl drop was carefully taken from the top of the bulk droplet and placed on the cantilever to avoid the generation of air bubbles when the head is placed. As it has been shown that micrometre-scale indenters lead to a better signal-to-noise ratio in comparison to their nano-scale counterparts[27]. For all experiments, SAA-SPH-5UM cantilevers (Bruker, Germany) made of Si_3N_4 with a hemispheric tip (23 µm height, 5.13 µm radius) were used. The calibration of the amplitude and the exact cantilever spring constant was determined with the thermal noise method[28]. The cantilever was passivated with 1% Pluronic (P2443) for 30 min to prevent the adhesion of droplets on the tip after measurements[29]. Condensates were indented with 0.3 nN force and a cantilever approaching with a constant velocity of 1 um/s. Acquired data was first processed by Bruker data analysis software and prepared for calculation of rheological parameters using a homemade Mathematica code (Mathematica 14.0, Wolfram). Size distribution analysis and calculation of the radius of condensates were done using ImageJ (https://imagej.nih.gov/) from the phase contrast images.

Confocal fluorescence imaging

Confocal fluorescence imaging was performed using a Nikon Ti2 inverted microscope with a Nikon C2plus confocal system and a Plan Apo VC 20x DIC N2 objective (NA = 0.75, WD = 1000 µm). Imaging was conducted with a Galvano scanner in one-way scan mode at 6.897x zoom. Excitation was achieved with 489 nm and 562 nm lasers for GFP and TYE-665, respectively, with emissions detected at 540 nm and 665 nm. The detector gain was set to 100 (GFP) and 70 (TYE-665), and the pinhole size was 40 µm. A brightfield transmission

detection (TD) channel was also acquired. Images (512 × 512 pixels) were acquired in three planes: GFP, TYE-665, and TD, with an exposure time of 1095.456 ms at a voxel size of 1×1×1 pixel^3. Image processing and analysis were performed using Fiji (ImageJ) version 2.14.0/1. TIFF-formatted images were used for quantitative and structural analysis without additional thresholding or scaling.

Results

UV Irradiation affects the phase separation behaviour and promotes arrested fusion droplets

We first explored the phase diagram of PLL/dT40 by varying concentrations of components and selected the 1:1 ratio with 30 µM concentration for subsequent analysis (Figures S1 and S2), as this condition produced droplets of convenient size for mechanical analysis and imaging. Prior to investigating the effects of UV irradiation, we characterized the baseline phase separation behavior of PLL/dT40 under varying salt conditions, from 0 M to 1 M. At the two extremes (0 M and 1 M KCl), no droplets were observed. We attribute the high salt result to strong electrostatic screening, which reduces the intermolecular interactions below the threshold required for phase separation. Conversely, at low salt, strong intermolecular interactions likely result in the formation of tight 1:1 heterodimers. However, the charge asymmetry (-40 vs. +150) means that these dimers have a strong positive net charge, which precludes further association. Intermediate salt concentrations allow for interactions that are sufficiently loose that the molecules can exchange interaction partners within a liquid environment[30,31]. In agreement with these expectations, intermediate salt concentrations promoted the formation of spherical condensate droplets of varying sizes, with the largest average droplet diameters consistently formed at 150 mM KCl concentration (Figures 1A and B), a condition used for the remainder of our study.

For UV treatment, samples were prepared and placed under a UVC lamp (UVP UVG-11, λ=254 nm) on the modified stand with 4 plastic pins to fix the position of the Petri dishes for all irradiation, ensuring reproducibility and uniform exposure (Figure 1C). Samples were prepared over a total of four hours, with UV illumination applied during the final 30 (+UV30) or 45 (+UV45) minutes of this period[32]. Immediately after irradiation, phase-contrast microscopy images were captured from the samples. Visual inspections of UV-irradiated samples showed droplets with elongated shapes. These changes became more pronounced in +UV45 samples, as shown by further elongation and an increased number of elongated

droplets in the field of view (Figure 1D, E). Indeed, extended UV exposure led to a higher occurrence of doublet and clustered configurations (Figure 1F), accompanied by a significant increase in droplet-droplet contact area, as measured by the neck diameter (L) (Figure 1G, H). Additionally, our particle analysis revealed a significantly lower circularity index of +UV45 samples compared to the +UV30 and control samples (Figure 1I). Our size distribution analysis of singlet droplets revealed that the control samples exhibited an exponential distribution (and not log-normal[33] or power law[34] behaviours), indicating a quench-then-coalesce mechanism[35,36]. However, the +UV30 samples, and more prominently the +UV45 samples, exhibited a remarkable shift to a power-law distribution, suggesting a transition to an addition of mass model[34] (Figure 1J and S3).

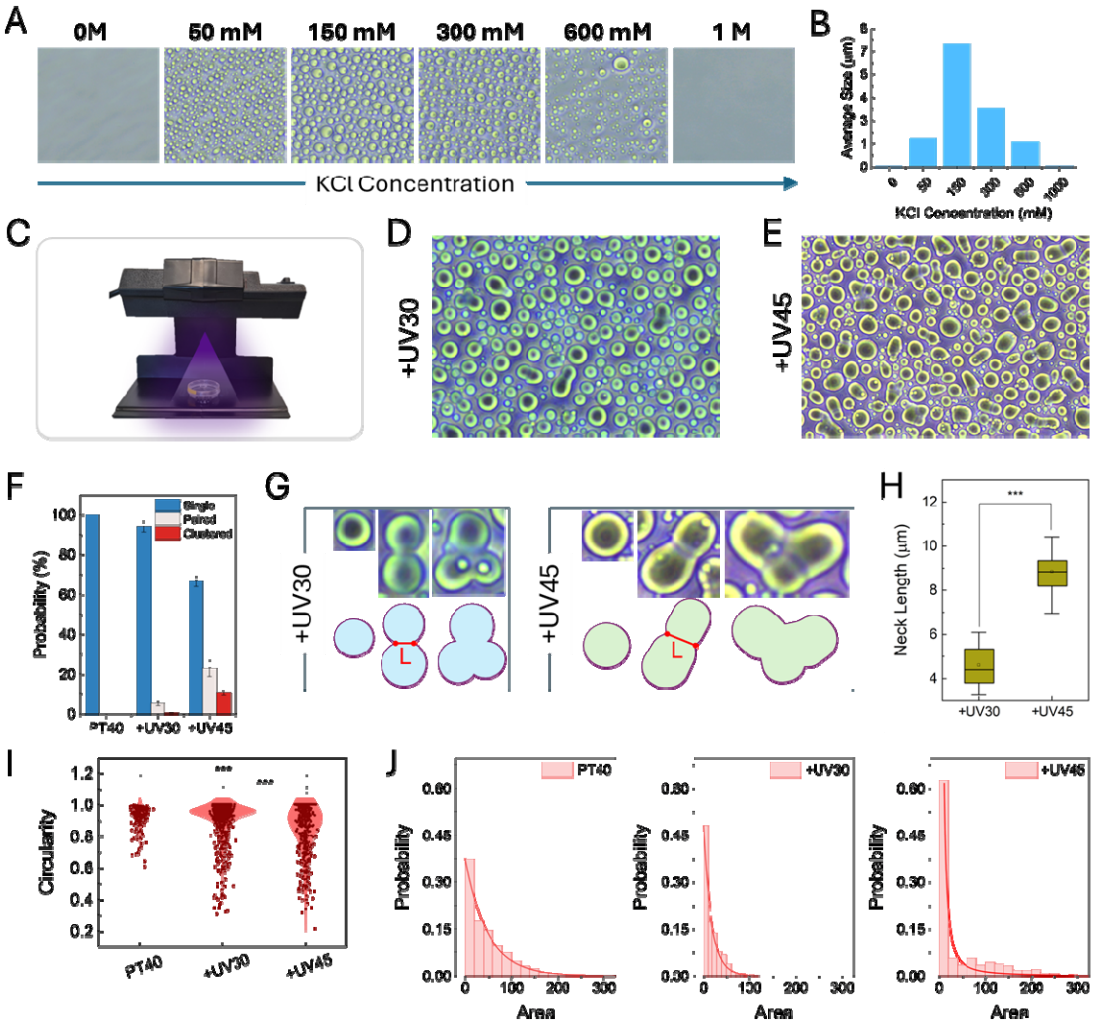

Figure 1. Experimental setup and morphological characterization of PLL:dT40 condensates with and without UV illumination. A) Effect of salt concentration on condensate formation. No condensates formed at extreme salt concentrations (0 M and 1 M KCl), while intermediate KCl concentrations resulted in the formation of droplets. B) Quantification of average droplet diameters at different salt concentrations. The highest average droplet diameter was recorded at 150 mM KCl. C) UV irradiation setup. UVC lamp installed on a modified stand ensured uniform exposure. All samples were placed in

a fixed position on the holder beneath the lamp. Images were captured after a total of 4 hours of sample preparation, including 30 and 45 minutes of UV irradiation at the final stages. D, E) Visual inspections showed clear morphological changes in the droplets after 30 and 45 minutes of UV exposure, with elongated droplets appearing after UV exposure. These elongations were more pronounced following 45 minutes of irradiation. F) Comparison of droplet morphologies after UV treatments. The longer UV exposure results in increased probability of doublet and clustered configurations formation and enhanced droplet–droplet contact, as evidenced by the larger interfacial areas measured as chord length (L) in doublets (G, H). I) Morphological analysis of the droplets by calculating the circularity parameter. Values range from 0 (irregular) to 1 (perfectly circular). J) Size distribution analysis of singlet droplets. Data are fitted by an exponential) and power-law ( ) curves.

Rheological analysis reveals liquid-to-solid transition upon UV exposure

Morphological and size distribution analyses prompted us to investigate whether UV exposure alters condensate mechanics. To address this, we performed oscillatory rheology measurements of the storage modulus (G′) and loss modulus (G″) on control and UV-illuminated samples using a recently developed SPM-based approach[10] (Figure 3A, Note S1). Across the entire frequency range examined (1 Hz to 100 Hz), G″ consistently exceeded G′, indicating that the control droplets exhibited predominantly viscous characteristics (Figure 2B).

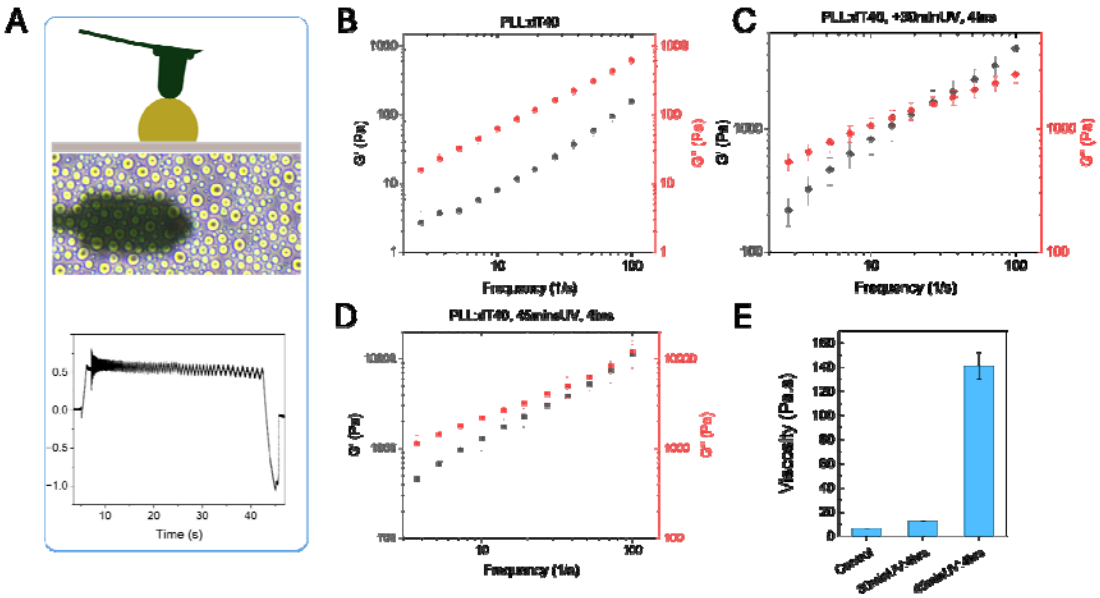

Figure 2. SPM based mechanical characterization of PLL:dT40 condensates under different conditions (control, +30 min treatment, +40 min treatment). A) Schematic of the experimental setup illustrating the scanning probe contacting a droplet deposited on a substrate. B) Frequency sweep of the storage modulus (G′, black) and loss modulus (G″, red) for the untreated (control) condensate, showing G″ > G′ across the tested frequency range (1 Hz to 100 Hz). C, D) Frequency sweep of G′ (black) and G″ (red) after UV irradiation. E) Viscosity values derived from the loss modulus (G″) under each condition, illustrating progressive increases in viscosity with extended irradiation durations.

Following UV treatment, significant changes in the viscoelastic responses were observed (Figure 3C). In +UV30 samples, G′ and G″ intersected around 20 Hz, reflecting a crossover in the mechanical behavior. At frequencies below 20 Hz, G′ and G″ both showed notable increases compared to the control, with G′ increasing from 5 Pa to around 300 Pa, and G″ growing from 20 Pa to about 600 Pa. Above 20 Hz, G′ rose more steeply, reaching about 4500 Pa at 100 Hz, while G″ reached about 2600 Pa. Consequently, G′ surpassed G″ at higher frequencies, consistent with an enhanced elastic response beyond the 20 Hz crossover point. In +UV45 samples (Figure 1D), a similar trend is seen, but the crossover is shifted to higher frequencies (f > 40 Hz), where differences between G′ and G″ become nonsignificant. This data indicates that by increasing UV exposure, elastic contributions (G′) were more pronounced than viscous contributions (G″) at higher frequencies. Finally, we measured the terminal viscosity of these condensates at T = 25°C (Figure 2E). Control samples had the lowest viscosity (6.2 ± 0.09 Pa.s), followed by +UV30 (12.08 ± 0.11 Pa.s), while +UV45 condensates showed the highest (140.77± 11.7 Pa.s).

UV irradiation significantly alters nucleation and coalescence processes

UV irradiation is known to promote intra-molecular interactions, particularly between two adjacent thymine nucleotides. However, it has also been proven, albeit with a lower probability, to induce non-adjacent and inter-chain interactions via dimer formation[32]. This competition between intra- and inter-chain interactions can significantly influence condensate formation and growth. To investigate this phenomenon, we conducted UV irradiation for 45 minutes under two conditions: the "Premix" condition, where UV illumination was applied to dT40 after the addition of buffer and before the addition of PLL, and the "0 hours" condition, where UV exposure was performed immediately after mixing dT40 and PLL. Interestingly, under the "0 hours" condition, we observed no condensate formation. Instead, a large network of interacting components was formed (Figure 3A, middle panel).

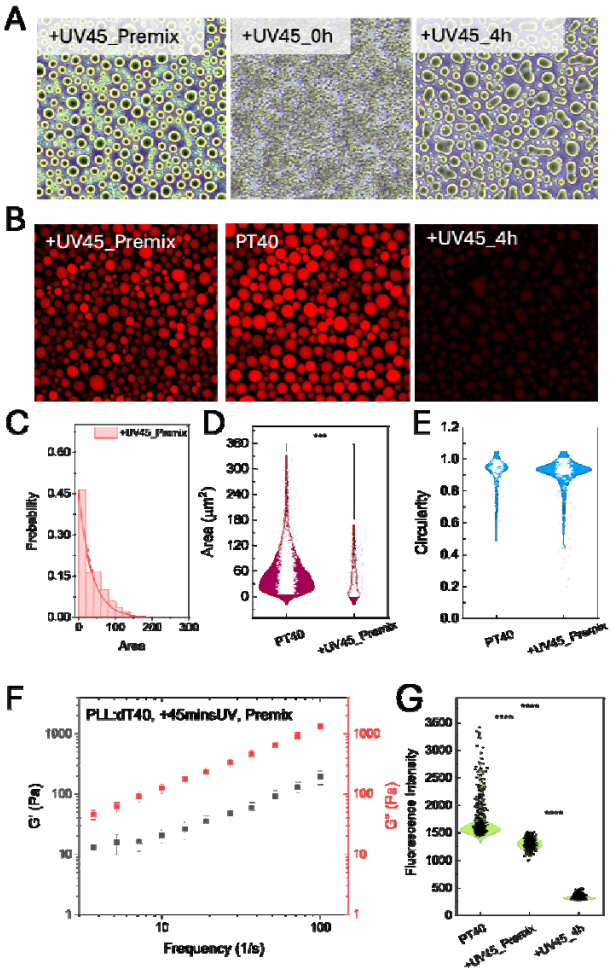

Figure 3. Condensation dramatically impacts the outcome of the UV-induced photochemical reaction in dT40/PLL solution. A, B) Representative phase contrast and confocal microscopy images show the results of the three different UV exposure protocols: premixing the DNA with buffer before adding PLL (+UV45_Premix), applying UV immediately after mixing (+UV45_0h), and irradiating at 4□h (+UV45_4h). Control samples with no UV illumination are represented as PT40. Early UV illumination (A, +UV45_0h) yields a percolated network rather than distinct droplets, whereas later irradiation (+UV45_4h) produces elongated but well-defined condensates. C) Size distribution analysis of droplets in +UV45_premix samples. Data are fitted by an exponential curve. D, E) Violin plots illustrate droplet morphology and size analysis. F) A frequency sweep of the storage modulus (G', red) and loss modulus (G'', black). This analysis showed no significant differences between control and premix samples. G) fluorescence intensity analysis of the droplets after addition of the fluorescently tagged dT40 DNA. +UV45_4h samples showed the lowest intensity, indicating minimum penetration of tagged DNA into the condensate. PT40 samples showed the highest exchange of DNA with the dilute phase as indicated by the highest intensity of fluorescence.

Interestingly, in premix condition, we observed condensate formation (Figure 3A, left), with smaller sizes (Figure 3D) and similar circularity to control droplets (Figure 3E), indicating no elongation or deformation. Furthermore, premix UV irradiation had minimal impact on condensate mechanics, compared to the control (Figure 3F), which may be attributed to the low occurrence of inter-chain interactions. Indeed, our exchange analysis revealed that the DNA molecules are minimally exchangeable in +UV45 and readily exchangeable in

+UV45_premix and control. To demonstrate this, we added 1% TYE-665 tagged dT40 to the dilute phase after condensate formation and imaged the droplets after an additional hour of incubation. As shown in Figure 3B, the +UV45_4h samples exhibited the lowest fluorescence intensity compared to both the premix and control samples, with control samples (which received no UV illumination) displaying the highest intensity (Figure 3G). Overall, our data fits a model in which optically regulated interplay between local or long-range intra-chain and inter-chain interactions leads to changes in condensate mechanics.

UV-stabilized droplets exhibit stability and internal compartmentalization

The above observations suggested that UV exposure cross-links DNA molecules in the condensates, thereby altering condensate mechanics and promoting the formation of arrested fusion droplets, which in turn affects chemical compartmentalization. To further assess stability and compartmentalization, we examined the response of +UV45 droplets to extreme changes in the surrounding environment. This was done by replacing the dilute phase with two extreme conditions that, according to our KCl concentration phase diagram, did not support droplet formation. To do this, following UV irradiation, we removed the original dilute phase and replaced it with pure water (0 M KCl) or an aqueous solution of 1 M KCl. In both cases, the condensates remained stable. In the case of 0 M KCl, Phase-contrast microscopy and confocal imaging with FITC-labeled PLL (green) and TYE-665-labeled dT40 (red) revealed the formation of dilute regions within the droplets, indicating an electrostatic-driven collapse of the dense network[37] (darker circles inside the droplets in Figures 4A-D). Washing thus revealed partial compartmentalization induced by UV illumination, which indicates that not all regions were uniformly crosslinked or equally stabilized.

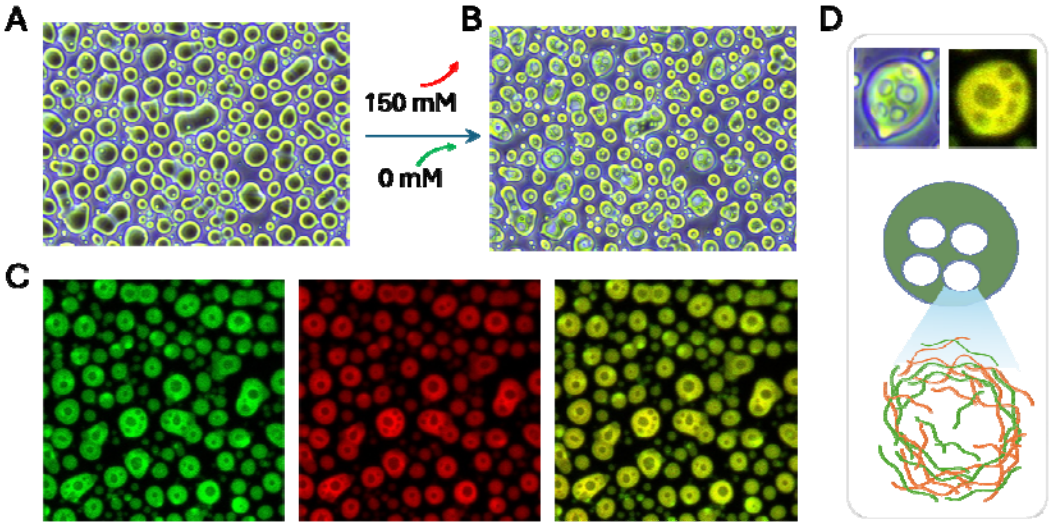

Figure 4. UV irradiated condensate droplets feature internal compartmentalization and remain stable upon drastic changes to the dilute phase. A) Phase-contrast images showing the morphology of +UV45 droplets before and (B) upon exchanging the dilute phase from 150 mM KCl to 0 M KCl. Droplets remained stable but exhibited internal heterogeneity upon this exchange. C) Confocal fluorescence images of +UV45 droplets with labelled FITC-PLL (green) and TYE-DNA (red) in 0 M KCl. D) Magnified view of representative droplets and schematic representation of single droplet, highlighting the observed internal compartmentalization.

Under 1M KCl condition, confocal fluorescence imaging showed an obvious decrease in the overall fluorescence intensity compared to droplets treated with pure water (Figure S4A and B). These findings point to a loss of fluorescence signal correlating with partial release or redistribution of molecular components within the highly charged environment, as expected due to the screening of electrostatic interactions. Additionally, unlike the PT40 droplets (Figure S5), fluorescence intensity line scans across an individual droplet revealed an interface with high fluorescence intensity (Figure S4 C) in both FITC and TYE channels.

Direct analysis of droplet fusion dynamics using SPM

Our previous morphological observations indicated that the fusion dynamics of droplets are significantly affected by UV-induced thymine dimerization. Next, we decided to directly quantify droplet-droplet interactions and fusion. For this aim, we developed a first-of-its-kind SPM-based assay for condensate droplet fusion and used it to conduct droplet–droplet interaction analyses on control and +UV45 samples. Figure 5A presents the experimental setup for this measurement. A dual-coated petri dish with BSA and Pluronic acid (PA), as described in detail in the methodology section, was used for making the condensate system. Droplets on the Pluronic-coated surfaces were less sticky and more spherical compared to the

BSA-coated side. This approach allowed us to easily capture a droplet, move to the BSA side to approach the target droplet, and perform a droplet-droplet fusion experiment (Figure 5B).

Our workflow begins by selecting a target droplet on the PA side, taking its image for later diameter calculation, and subsequently capturing it by the cantilever. The cantilever approaches the target droplet with a set force of 0.2 nN and a waiting time of 0 seconds, which is sufficient for the droplet to attach to the cantilever. Next, the cantilever is moved to the BSA side, adjacent to the target droplet. After capturing an image, the cantilever is positioned over the droplet to align the centers of the two droplets as precisely as possible. This step is followed by moving the cantilever towards the droplet on the surface with a constant velocity of 1 µm/s (Figure 1B), and force-time traces are recorded.

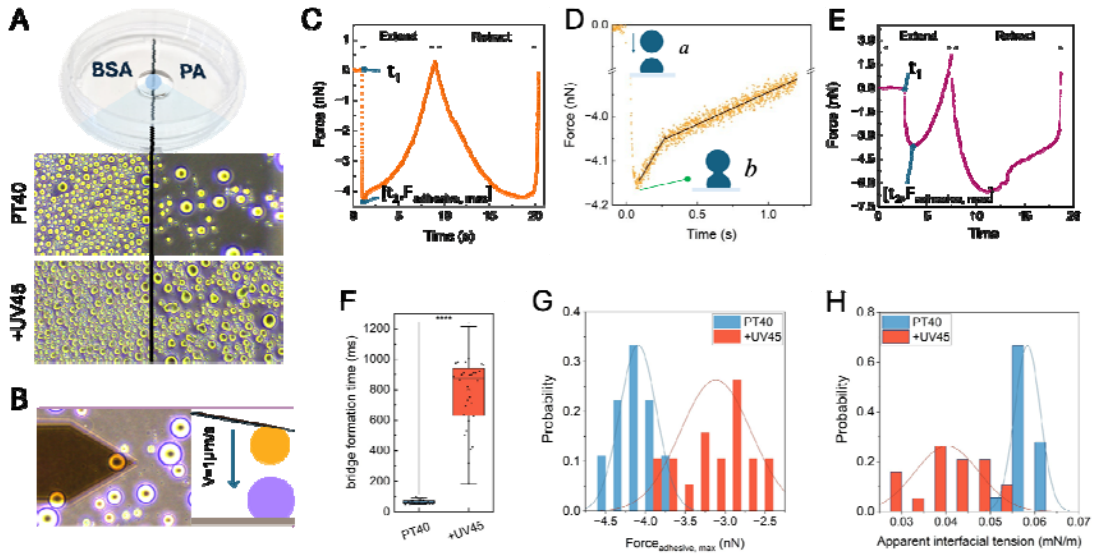

Figure 5. SPM-based droplet–droplet interaction analysis reveals UV-induced changes in fusion dynamics. A) Dual-area coated dish for condensate preparation. Comparison of droplet behavior on a dual-coated Petri dish with BSA (left) and Pluronic acid (PA; right) surfaces. The black line divides the two coated regions. The lower panels illustrate the differences in droplet formation: droplets on the PA side are more rounded and exhibit reduced stickiness compared to the BSA side, where droplets adhere more strongly to the surface. B) experimental setup for droplet-droplet interaction analysis using SPM. C) Representative example of the recorded Force-time curve for liquid-like PT40 droplets. A cycle includes an extend phase and a retraction phase. During the extend, the piezoelectric actuator is extended, moving the cantilever tip toward the sample surface. The cantilever, with an attached droplet, was moved downward (Extend phase) at 1 µm s⁻¹ until it contacted the droplet on the substrate, forming a liquid bridge. Following initial contact, the cantilever continues to move downward and compresses the bridge and fused droplets before retracting to its original position. The negative portion of the force curve indicates capillary attraction (adhesion) due to the liquid bridge. D) Zoomed in force–time trace showing the interactions between two liquid-like PT40 droplets. The force remains near zero before contact (a), rapidly drops to a negative minimum upon bridge formation (b), and then transitions through two distinct regimes of coalescence and droplet reshaping. The presence of these two regimes suggests an initial rapid bridge expansion followed by a slower phase, expectedly influenced by contact-line dynamics and substrate wetting. E) Representative Force-time trace for +UV45 sample. (F) Box plot comparing the bridge formation times (t_2-t_1) for PT40 and +UV45 samples. The +UV45 sample shows a significantly longer bridge formation time. G) Maximum adhesive force ($_{adhesive,\ max}$) during droplet interaction for PT40 and +UV45. The +UV45 sample shows a shift toward lower adhesive forces, suggesting that photo crosslinking alters the capillary interactions between droplets by increasing structural resistance to deformation. H) Apparent interfacial tension (γ) extracted from force–time traces for PT40 and +UV45.

Figure 5C shows a typical force–time measurement recorded during the interaction of two liquid droplets under the SPM at a constant "extend" velocity of 1 μm s^{-1}. Initially, the force remains near zero, indicating that the droplets are not yet in contact. As the cantilever moves downward, the force rapidly shifts (starting at t_1) to a negative (adhesive) regime when the droplets first come into contact and form a liquid bridge (t_2). We call the time duration between these two events as liquid bridge formation time (t_2-t_1). Following this step, the cantilever continues to move downward at the same speed after bridge formation, and the upper droplet is pressed against the substrate droplet, promoting the complete fusion. The liquid droplets then merge into a single droplet on the substrate. During the subsequent retract phase, the cantilever moves away from the surface, and the force profile remains in the adhesive regime until the connection between the cantilever and merged droplets ultimately breaks. As a result, the cantilever is effectively "dry" when it returns to its original position, while an enlarged droplet remains on the substrate.

Notably, our data revealed a significant difference in the force-time profiles of UV-treated and untreated samples. In non-crosslinked liquid-like droplets, the force drops instantly and then exhibits a two-stage recovery (Figure 5D) after reaching the negative minimum: an initial rapid increase due to fast bridge expansion, followed by a slower phase associated with droplet relaxation and substrate wetting. In these liquid-like droplets, strong capillary forces generated by surface tension primarily drive fusion, resulting in higher adhesive force (Figure 5G) and significantly shorter bridge formation times (Figure 5F). By contrast, in +UV45 droplets with gel-like behavior, the force decreases gradually, and the distinct two-regime behavior is absent; instead, the force recovery occurs gradually and in a continuous manner (Figures 5E, S6). This suggests that altered fusion dynamics result from reduced interface mobility due to UV-mediated DNA crosslinking and the need for polymer network rearrangement, which mediates fusion. Consequently, the significant viscous and elastic behaviors of these gel-like droplets delay droplet deformation and capillary bridge formation, slowing the fusion process in +UV45 droplets compared to PT40.

The fusion of phase-separated droplets is typically governed by the interplay between capillary forces and viscous dissipation, with fusion time often scaling with droplet size as predicted by previous studies on coalescence dynamics in simple fluid[38]. Consistent with this, we observed a positive correlation between droplet diameter and bridge formation time (Figure S7), supporting the size-dependent nature of fusion. To further quantify the magnitude of the adhesive forces driving droplet fusion, we estimated the apparent interfacial

tension (γ) using the standard capillary-force approximation. This approximation relates the maximum attractive capillary force observed during droplet approach (which we will refer to as $F_{adhesive,\ max}$) to the apparent interfacial tension and the reduced radius (R^*) of the droplets, according to the equation:

$$F_{adhesive,\ max} \approx 4\pi\gamma R^*$$

The $F_{adhesive,\ max}$ was directly obtained from the maximum adhesive force (absolute value) recorded in the extend phase of the force-time curves. The reduced radius (R^*) was calculated from the radii of the two interacting droplets, using the equation below:

$$R^* = \frac{R_1 R_2}{R_1 + R_2}$$

Droplet radii were measured from microscopy images before SPM measurements, yielding radii of R_1 and R_2 for the droplets attached to the cantilever and on the substrate, respectively.

Measurements of maximum adhesive force (Figure 5H) showed a reduction in +UV45 droplets compared to PT40, suggesting weaker liquid bridge interactions, likely due to increased viscoelasticity as also was proven by our mechanical analysis. Additionally, the apparent interfacial tension (Figure 5I) exhibited a broader and slightly shifted distribution in +UV45 samples, reflecting changes in interfacial properties that may arise from crosslinking-induced modifications to the droplet surface. Collectively, our data revealed that while UV irradiation significantly altered the kinetics and mechanical response of droplet fusion by introducing structural rigidity that resists rapid deformation.

Discussion

Mechanics of phase-separated biomolecular condensate droplets can be altered in various ways, including by changing their chemistry, internal structure, or environmental temperature. Here, we showed how light can be leveraged to program the connectivity and internal organization of a nucleic acid-based condensate system, thereby changing condensate mechanics with minimal alterations to chemical content. The study revealed that UV irradiation may suppress or stabilize condensation through the formation of covalent intra- and interchain contacts (Figure 6), with dramatic implications for droplet morphology, structural mechanics, and fusion dynamics. While control droplets remained mostly viscous

(G″ > G′), UV illumination led to the emergence of an elastic-like component with a dramatic increase in G′, reaching values consistent with solid-like or gel-like materials at higher frequencies[39]. This shift suggests that extended UV illumination enhances intermolecular interactions that restrict molecular mobility and reinforce the droplet environment, reflecting observations in other phase-separated systems undergoing gelation or enhanced crosslinking[40,41].

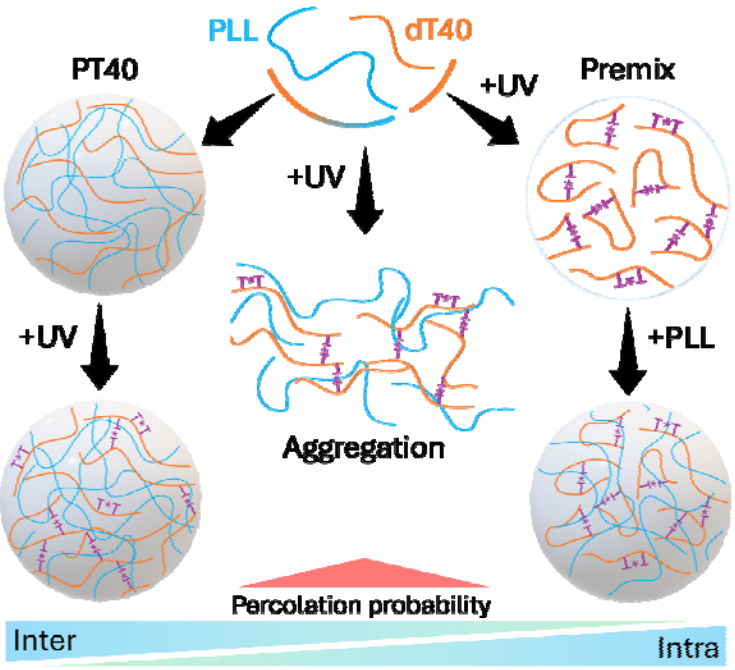

Figure 6. Reciprocal interplay between photochemical reactions and condensation, governed by shifts in inter- and intra-chain interactions. Our data indicate the dominant role of the intra-molecular interactions in premix conditions, which decreases in samples exposed to UV after condensates formed, mainly due to the presence of interacting partners in the environment and increases in dT40 gyration radius that dominated inter-molecular interactions. Between the two extremes, UV irradiation leads to the formation of a percolated network of interacting polymers in 0-hour condition, which results in the formation of aggregates with globally connected chains. The red triangle denotes an increased probability of network percolation in 0-hour UV-illuminated samples.

Our study presented a clear example in which a photochemical process is modulated by condensation. Irradiating the system immediately after mixing the building blocks bypassed typical droplet formation and instead yielded a network-like structure, suggesting that early nucleation events were crosslinked before droplets could coalesce, promoting the formation of percolated architectures[42]. In contrast, applying UV after droplets had formed led to rearrangements primarily within the droplet interior. Premix condition, where the nucleic acid

was irradiated prior to adding PLL, produced smaller droplets that retained a largely viscous profile, presumably because intra-strand bond formation dominated in the absence of the polypeptide partner, limiting the interaction sites for PLL to form larger complexes and grow. Overall, the outcome of light-induced thymine dimerization shows dependency on whether DNA is in a condensed phase or not. Our observations can be explained knowing that condensation affects the radius of gyration of polymers as well as the density and inter-chain contact probability [8,43–45], which will in turn regulate the occurrence of short-range and long-range intra-chain and inter-chain thymine dimers.

Our finding provides insights into the role that UV illumination may have played in the origin of life. Early Earth conditions likely exposed primitive protocells to variable doses of solar UV radiation, which could have simultaneously driven molecular crosslinking (through pyrimidine dimerization in early nucleic acids[46,47]) while also posing a threat to nucleic acid stability[48]. Recent models suggest that compartmentalization may have offered a protective niche, protecting nascent genetic material from harmful UV doses[49]. Notably, our findings reveal that UV illumination induces compartmentalization and enhances the stability of the coacervate droplets against drastic changes in environmental chemistry. This mechanism may have played a key role in the resilience and evolution of early biopolymeric systems, balancing the harmful and beneficial effects of radiation on the development of life-like systems.

This study provides new tools and approaches for the synthesis and characterization of materials. The presented SPM assay for droplet fusion analysis enables studying condensate fusion dynamics in physiological and pathological settings. Furthermore, the synthesis of stabilized condensate droplets with tunable mechanical properties may open new avenues in materials and particle synthesis, for biomedical and engineering applications. Such tunability offers exciting opportunities for the design of programmable biomolecular materials, especially given the noninvasive nature of UV-induced crosslinking[50]. The approach presented in this study is versatile and can be readily applied to other polyelectrolyte–nucleic acid systems or under different environmental conditions. It thus opens avenues for engineering synthetic organelles and soft materials that dynamically respond to changes in their environment.

Acknowledgments

The authors thank Kostas Tassis (Leiden University) for his assistance with microscopy.

Author Contributions

Conceptualization, A.M. and V.S.; methodology, A.M. and V.S.; investigation, V.S., A.M., D.B., J.S.; visualization, V.S.; formal analysis, V.S. and F.W.; writing – original draft, V.S. and A.M.; writing – review & editing, V.S., A.M., J.S., D.B., F.W.; project administration, funding acquisition, and supervision, A.M.

Declaration of Interests

The authors have no conflicting interests to disclose.

References

1. Banani, S. F., Lee, H. O., Hyman, A. A. & Rosen, M. K. Biomolecular condensates: organizers of cellular biochemistry. *Nat Rev Mol Cell Biol* **18**, 285–298 (2017).

2. Shin, Y. & Brangwynne, C. P. Liquid phase condensation in cell physiology and disease. *Science (1979)* **357**, 1253–1253 (2017).

3. Dao, T. P. *et al.* Ubiquitin Modulates Liquid-Liquid Phase Separation of UBQLN2 via Disruption of Multivalent Interactions. *Mol Cell* **69**, 965-978.e6 (2018).

4. Sabari, B. R. *et al.* Coactivator condensation at super-enhancers links phase separation and gene control. *Science (1979)* **361**, 379–379 (2018).

5. Evers, T. M. J., Holt, L. J., Alberti, S. & Mashaghi, A. Reciprocal regulation of cellular mechanics and metabolism. *Nat Metab* **3**, 456–468 (2021).

6. Dignon, G. L., Best, R. B. & Mittal, J. Biomolecular Phase Separation: From Molecular Driving Forces to Macroscopic Properties. *Annu Rev Phys Chem* **71**, 53–75 (2020).

7. Muzzopappa, F., Hertzog, M. & Erdel, F. DNA length tunes the fluidity of DNA-based condensates. *Biophys J* **120**, 1288–1300 (2021).

8. Heidari, M., Moes, D., Schullian, O., Scalvini, B. & Mashaghi, A. A topology framework for macromolecular complexes and condensates. *Nano Res* **15**, 9809–9817 (2022).

9. Boeynaems, S. *et al.* Protein Phase Separation: A New Phase in Cell Biology. *Trends Cell Biol* **28**, 420–435 (2018).

10. Naghilou, A., Armbruster, O. & Mashaghi, A. Scanning probe microscopy elucidates gelation and rejuvenation of biomolecular condensates. *Cell Rep Phys Sci* **6**, 102430 (2025).

11. Johnson, A. T. & Wiest, O. Structure and dynamics of poly(T) single-strand DNA: Implications toward CPD formation. *Journal of Physical Chemistry B* **111**, 14398–14404 (2007).

12. Douki, T., Laporte, G. & Cadet, J. Inter-strand photoproducts are produced in high yield within A-DNA exposed to UVC radiation. *Nucleic Acids Res* **31**, 3134–3142 (2003).

13. Zhang, H. Mechanisms of mutagenesis induced by DNA lesions: multiple factors affect mutations in translesion DNA synthesis. *Crit Rev Biochem Mol Biol* **55**, 219–251 (2020).

14. Mao, P., Wyrick, J. J., Roberts, S. A. & Smerdon, M. J. UV□Induced DNA Damage and Mutagenesis in Chromatin. *Photochem Photobiol* **93**, 216–228 (2017).

15. Pfeifer, G. P. & Besaratinia, A. UV wavelength-dependent DNA damage and human non-melanoma and melanoma skin cancer. *Photochemical & Photobiological Sciences* **11**, 90–97 (2012).

16. Sinha, R. P. & Häder, D. P. UV-induced DNA damage and repair: A review. *Photochemical and Photobiological Sciences* **1**, 225–236 (2002).

17. Zhao, C., Snellman, E., Jansen, C. T. & Hemminki, K. In situ repair of cyclobutane pyrimidine dimers in skin and melanocytic nevi of cutaneous melanoma patients. *Int J Cancer* **98**, 331–334 (2002).

18. Nakashima, K. K., van Haren, M. H. I., André, A. A. M., Robu, I. & Spruijt, E. Active coacervate droplets are protocells that grow and resist Ostwald ripening. *Nat Commun* **12**, (2021).

19. Masukawa, M. K. *et al.* Water□in□Water Droplets Selectively Uptake Self□Assembled DNA Nano/Microstructures: a Versatile Method for Purification in DNA Nanotechnology. *ChemBioChem* **23**, (2022).

20. Lechuga, I. & Michaelian, K. Fatty Acid Vesicles as Hard UV-C Shields for Early Life. *Foundations* **3**, 99–114 (2023).

21. Erkamp, N. A. *et al.* Dynamically arrested condensate fusion creates complex structures with varying material properties. Preprint at https://doi.org/10.1101/2024.11.15.623768 (2024).

22. Elbaum-Garfinkle, S. *et al.* The disordered P granule protein LAF-1 drives phase separation into droplets with tunable viscosity and dynamics. *Proceedings of the National Academy of Sciences* **112**, 7189–7194 (2015).

23. Ghosh, A., Kota, D. & Zhou, H. X. Shear relaxation governs fusion dynamics of biomolecular condensates. *Nat Commun* **12**, (2021).

24. Roggeveen, J. V., Wang, H., Shi, Z. & Stone, H. A. A calibration-free model of micropipette aspiration for measuring properties of protein condensates. *Biophys J* **123**, 1393–1403 (2024).

25. Wang, H., Kelley, F. M., Milovanovic, D., Schuster, B. S. & Shi, Z. Surface tension and viscosity of protein condensates quantified by micropipette aspiration. *Biophysical Reports* **1**, 100011 (2021).

26. Meyer, E., Jarvis, S. P. & Spencer, N. D. Scanning Probe Microscopy in Materials Science. *MRS Bull* **29**, 443–448 (2004).

27. Glaubitz, M. *et al.* A novel contact model for AFM indentation experiments on soft spherical cell-like particles. *Soft Matter* **10**, 6732–6741 (2014).

28. Sader, J. E., Chon, J. W. M. & Mulvaney, P. Calibration of rectangular atomic force microscope cantilevers. *Review of Scientific Instruments* **70**, 3967–3969 (1999).

29. Vidal Ceballos, A. *et al.* Liquid to solid transition of elastin condensates. *Proceedings of the National Academy of Sciences* **119**, (2022).

30. Muthukumar, M., Hua, J. & Kundagrami, A. Charge regularization in phase separating polyelectrolyte solutions. *Journal of Chemical Physics* **132**, (2010).

31. Li, L. *et al.* Phase Behavior and Salt Partitioning in Polyelectrolyte Complex Coacervates. *Macromolecules* **51**, 2988–2995 (2018).

32. Nagpal, A. *et al.* Thymine dissociation and dimer formation: A Raman and synchronous fluorescence spectroscopic study. *Proc Natl Acad Sci U S A* **118**, (2021).

33. L'Estimé, M., Schindler, M., Shahidzadeh, N. & Bonn, D. Droplet Size Distribution in Emulsions. *Langmuir* **40**, 275–281 (2024).

34. Brangwynne, C. P., Mitchison, T. J. & Hyman, A. A. Active liquid-like behavior of nucleoli determines their size and shape in Xenopus laevis oocytes. *Proc Natl Acad Sci U S A* **108**, 4334–4339 (2011).

35. Kim, J., Han, K. Y., Khanna, N., Ha, T. & Belmont, A. S. Nuclear speckle fusion via long-range directional motion regulates speckle morphology after transcriptional inhibition. *J Cell Sci* **132**, (2019).

36. Lee, D. S. W., Wingreen, N. S. & Brangwynne, C. P. Chromatin mechanics dictates subdiffusion and coarsening dynamics of embedded condensates. *Nat Phys* **17**, 531–538 (2021).

37. Erkamp, N. A. *et al.* Spatially non-uniform condensates emerge from dynamically arrested phase separation. *Nat Commun* **14**, 684 (2023).

38. Yue, H., Burton, J. C. & Sussman, D. M. Coalescing clusters unveil regimes of frictional fluid mechanics. *Phys Rev Res* **6**, (2024).

39. Makarova, A. O. *et al.* Supramolecular Structure and Mechanical Performance of κ-Carrageenan–Gelatin Gel. *Polymers (Basel)* **14**, 4347 (2022).

40. Murthy, A. C. *et al.* Molecular interactions underlying liquid−liquid phase separation of the FUS low-complexity domain. *Nat Struct Mol Biol* **26**, 637–648 (2019).

41. Dignon, G. L., Zheng, W., Kim, Y. C. & Mittal, J. Temperature-Controlled Liquid-Liquid Phase Separation of Disordered Proteins. *ACS Cent Sci* **5**, 821–830 (2019).

42. Ryan, V. H. *et al.* Mechanistic View of hnRNPA2 Low-Complexity Domain Structure, Interactions, and Phase Separation Altered by Mutation and Arginine Methylation. *Mol Cell* **69**, 465-479.e7 (2018).

43. Heidari, M., Schiessel, H. & Mashaghi, A. Circuit Topology Analysis of Polymer Folding Reactions. *ACS Cent Sci* **6**, 839–847 (2020).

44. Farag, M., Borcherds, W. M., Bremer, A., Mittag, T. & Pappu, R. V. Phase separation of protein mixtures is driven by the interplay of homotypic and heterotypic interactions. *Nat Commun* **14**, 5527 (2023).

45. Bauer, D. J. & Nikoubashman, A. The conformations of protein chains at the interface of biomolecular condensates. *Nat Commun* **15**, 9975 (2024).

46. Crucilla, S. J. *et al.* UV-driven self-repair of cyclobutane pyrimidine dimers in RNA. *Chemical Communications* **59**, 13603–13606 (2023).

47. Climent, T., González-Ramírez, I., González-Luque, R., Merchán, M. & Serrano-Andrés, L. Cyclobutane Pyrimidine Photodimerization of DNA/RNA Nucleobases in the Triplet State. *J Phys Chem Lett* **1**, 2072–2076 (2010).

48. Rastogi, R. P., Richa, Kumar, A., Tyagi, M. B. & Sinha, R. P. Molecular Mechanisms of Ultraviolet Radiation□Induced DNA Damage and Repair. *J Nucleic Acids* **2010**, (2010).

49. Strulson, C. A., Molden, R. C., Keating, C. D. & Bevilacqua, P. C. RNA catalysis through compartmentalization. *Nat Chem* **4**, 941–946 (2012).

50. Choi, J.-M., Holehouse, A. S. & Pappu, R. V. Physical Principles Underlying the Complex Biology of Intracellular Phase Transitions. *Annu Rev Biophys* **49**, 107–133 (2020).